High Power Sodium-Ion Batteries and Hybrid Electrochemical Capacitors Using Mo or Nb-Doped Nano-Titania Anodes

Dustin Bauer,[1,2] Alexander J. Roberts,[3] Sai Gourang Patnaik,[2] Dan J. L. Brett, [4] Paul R. Shearing, [4] Emma Kendrick, [3,4] Noriyoshi Matsumi, [2,*] and Jawwad A. Darr [1,z]

[1]*Department of Chemistry, University College London, London WC1H 0AJ, United Kingdom*
[2]*School of Materials Science, Japan Advanced Institute of Science and Technology, Nomi, Ishikawa, Japan*
[3]*WMG, University of Warwick, CV4 7AL Coventry, United Kingdom*
[4]*Electrochemical Innovation Lab, Department of Chemical Engineering, University College London, London WC1E 7JE, United Kingdom*

Nano-sized anatase (TiO_2) and doped anatase ($Mo_{0.1}Ti_{0.9}O_2$ and $Nb_{0.25}Ti_{0.75}O_2$) materials (ca. 5 nm) were synthesized using continuous hydrothermal flow synthesis and evaluated as negative electrodes in Na-ion batteries and hybrid capacitors. Na-ion half-cells (vs. Na metal counter electrodes) for the Mo-doped titania ($Mo_{0.1}Ti_{0.9}O_2$) and Nb-doped titania ($Nb_{0.25}Ti_{0.75}O_2$) electrodes both showed significantly higher specific discharge capacities than undoped anatase (ca. 75 mAh g^{-1} compared to only 30 mAh g^{-1} for undoped TiO_2 at 1 A g^{-1}). This improved performance was attributed to higher pseudocapacitive contributions to charge storage, as well as improved sodium ion diffusion and lower charge transfer resistance. Na-ion hybrid electrochemical capacitors (Na-HECs) were made from the electrodes with activated carbon positive electrodes. As expected, Na-HECs using doped titania showed superior performance to the undoped anatase, with power densities up to 10.5 kW kg^{-1} or energy densities of over 60 Wh kg^{-1} (based on the weight of active material in both anode and cathode). The $Mo_{0.1}Ti_{0.9}O_2$/AC Na-ion hybrid capacitor also showed excellent specific capacitance retention of ca. 75% over 3000 cycles at 5 mA cm^{-2} (1 A g^{-1}).
© The Author(s) 2018. Published by ECS. This is an open access article distributed under the terms of the Creative Commons Attribution 4.0 License (CC BY, http://creativecommons.org/licenses/by/4.0/), which permits unrestricted reuse of the work in any medium, provided the original work is properly cited. [DOI: 10.1149/2.0341809jes]

Energy storage has become an ever-more relevant field of research in recent years, as (hybrid) electric vehicles, grid energy-storage and portable electronics have become increasingly important.[1,2] Since the commercialization of rechargeable Li-ion batteries by Sony in 1991, they have become the most widespread type of energy storage in portable devices due to their high energy densities and minimal self-discharge.[3] However, there are some concerns about the availability of supply and the associated cost of lithium,[4] as demand for Li-ion batteries (LIBs) continues to rise. Especially for stationary applications, such as grid storage, Na-ion battery (NIB) technology has been gaining interest both in academic and commercial research because of its high natural abundance and widespread availability in seawater.[5]

Expertise from LIB research can be readily transferred to NIBs, thereby accelerating progress.[6] Possible active materials for NIB negative electrodes include hard carbons,[7,8] alloying materials such as Sn/carbon composites,[9,10] conversion materials such as $NiCo_2O_4$,[11] as well as titanium-based insertion materials. The various polymorphs of TiO_2 have received a great deal of attention, including amorphous nanotubes,[12,13] TiO_2(B),[14,15] rutile,[5] Nb-doped,[16] N/S co-doped,[17] as well as undoped anatase TiO_2.[4,6]

One of the disadvantages of LIBs and NIBs is their typically inferior performance at high power compared with supercapacitors. Therefore, for applications such as regenerative braking, which require the ability to store charge rapidly, electrochemical double layer capacitors (EDLC) are considered promising.[18] In EDLCs, charge is built up at the electrode/electrolyte interface by the movement of solvated ions in the electrolyte to the surface of the electrode of the opposing charge. The main issues with EDLCs, however, are their limited energy densities and rapid self-discharge,[19] which could be mitigated by developing hybrid electrochemical capacitors (HECs), which employ a combination of an EDLC electrode (typically made of high surface area carbon) and a battery-type electrode.

During the charging of a Na-ion hybrid electrochemical capacitor (Na-HEC), sodium cations are inserted into the active material in the anode, whereas anions (often hexafluorophosphate) are adsorbed onto the active carbon in the cathode. $[PF_6]^-$ desorption and Na$^+$ extraction are observed during discharge.[20] In contrast to metal-ion

batteries, in HECs there are symmetrical driving forces for cations and anions to migrate to opposite electrodes during charge and discharge.[21] Therefore, concentration gradients are reduced, and better high rate performance is to be expected in Na-HECs compared to NIBs.[22] The ideal case would be to develop HECs that can deliver both high power and energy densities simultaneously.

Various TiO_2 polymorphs have been shown to exhibit extrinsic pseudocapacitive behavior in Na-ion half cells, including amorphous nanotubes,[12] anatase TiO_2/TiO_2(B)-graphene composites,[14] and anatase TiO_2 mesocages.[23] The surface or near-surface, faradaic, highly-reversible redox reactions which are the basis of extrinsic pseudocapacitance allow for much faster charge storage than diffusion-controlled intercalation processes, therefore enabling faster charge/discharge.[24] When materials such as TiO_2 are nanosized, diffusion occurs only on very short distances,[25] and once crystallite size falls below a critical limit, surface sites to accommodate Li$^+$ or Na$^+$ become available for fast faradaic reactions in a range of energies.[24,26] This has been described as the surface of the nanomaterial acting as solid-solution host for Li-ion insertion,[27] and can equally be expected for Na-ion storage. Thus, nano-titania based materials could be suitable as active materials for anodes in Na-HECs. Na-HECs with activated carbon positive electrodes have previously been constructed using a variety of anodes, including $NiCo_2O_4$,[28] sodium titanate nanotubes,[29] and $Na_4Mn_9O_{18}$.[30]

The heterometallic doping of TiO_2 with cations of a higher valence than Ti(IV) has previously been reported to improve the performance of anatase in energy storage applications. The electronic conductivity was expected to improve with the inclusion of Mo^{6+} or Nb^{5+} in the crystal lattice,[31,32] via the introduction of conduction band electrons, oxygen defects, and titanium vacancies.[33] In contrast, hydrogenation has been used to reduce the valence state of titanium in TiO_2 to Ti(III) to introduce oxygen vacancies, but the improvements in electrochemical performance and electronic conductivity were limited.[34] Both Mo-doping and Nb-doping have been shown to improve the electrochemical performance of anatase for energy storage applications via the expansion of the lattice.[16,31,32,35] Nb-doped anatase has previously been investigated as a transparent conductive oxide due to its high electrical conductivity.[36]

Herein, we demonstrate that doped TiO_2 nanoparticles synthesized via a highly scalable continuous hydrothermal flow process can be used as active materials for negative electrodes both in NIBs as

Table I. Synthesis conditions for the doped and undoped TiO₂ samples.

	T_{heater} [/°C]	T_{mix} [/°C]	Pump 2	Pump 3
TiO₂	400	305	0.3 M TiBALD	DI water
Mo₀.₁Ti₀.₉O₂			0.45 M TiBALD	
	450	335	0.05 M $(NH_4)_6Mo_7O_{24}$ · $4H_2O$	0.3 M KOH
Nb₀.₂₅Ti₀.₇₅O₂			0.4 M TiBALD	
	450	335	0.1 M $C_4H_4NNbO_9$.	0.3 M KOH

well as high-performance Na-HECs. Because of higher pseudocapacitive charge storage contributions (observed from scan rate testing), electrodes using either Mo-doped or Nb-doped TiO₂ performed significantly better than the undoped equivalent at high charge/discharge rates in Na-ion half-cells and Na-HECs.

Experimental

Synthesis.—Nano-sized TiO₂, molybdenum-doped TiO₂ and niobium-doped TiO₂ were synthesized using a continuous hydrothermal flow synthesis (CHFS) process, which has previously been described by some of the authors at both the pilot[37] and lab scales.[38–40] A schematic of the reactor can be found in the Electronic Supplementary Information (ESI, see Figure S1). The CHFS process involved the mixing of a feed of supercritical water and a second ambient temperature flow of aqueous metal salts (precursors for the materials) inside a patented co-current Confined Jet Mixer (CJM) made from off-the-shelf Swagelok parts.[38] The instant mixing under extreme conditions results in the formation of high surface area metal oxides. The simplified general synthetic route as described in the literature involves a set of reactions including the hydrolysis and dehydration of metal salts.[38] This neglects the decomposition of anions and multiple complex steps involved in the hydrolysis, but it can serve to illustrate the simplified synthetic route.

The synthesis of all three materials has been described previously by the authors.[32,35] The synthesis conditions for the three samples can be found in Table I. The CHFS residence time was ca. 5 seconds for all samples. Details for the method of clean-up and freeze-drying can be found in the Electronic Supplementary Information (ESI). The as-synthesized, freeze-dried powders were used without further treatment and were obtained as free flowing powders.

Physical characterization.—Powder X-ray diffraction (PXRD) patterns in a 2θ range of 10 to 40° were collected with a step size of 0.5°, and a step time of 20 s on a STOE StadiP diffractometer using Mo–Kα1 radiation (λ = 0.7093 Å).

High-resolution transmission electron microscopy (TEM) using a JEOL JEM 2100 – LaB₆ filament was used to determine size, interlayer spacing, and particle morphology. A Gatan Orius digital camera was used for image capture of the samples, which were pipetted onto a 300-mesh holey carbon copper film grid (Agar Scientific, Stansted, UK). Energy dispersive X-ray spectroscopy (EDX) was performed on the same JEOL JEM 2100 and used for the elemental analysis of the samples.

The valence states of the metal ions were determined using X-ray photoelectron spectroscopy (XPS) collected on a Thermo Scientific K-alpha spectrometer using Al-Kα radiation (λ = 0.8340 Å). High-resolution regional scans for Ti, Mo and Nb were conducted at 50 eV. Processing of the XPS data was performed using CasaXPS software (version 2.3.16) by calibrating the spectra using the C 1s peak at 284.8 eV.

Raman spectroscopy was performed using a HORIBA-JY T64000 triple monochromator with a 1800 gr mm⁻¹ grating. An Ar⁺ laser was used as excitation source for the 514.5 nm emission with a power of 5 mW.

Characterization of the texture of the materials was carried out using a Micrometrics Tristar II. The nitrogen adsorption and desorption isotherms were recorded at 77 K (liquid N₂). The Brunauer-Emmett-Teller (BET) method was used to calculate the specific surface areas of the materials and the pore size distributions were determined from the adsorption branch of the isotherm using the Barrett-Joyner-Halenda (BJH) method.

The tap density of the as-synthesized powders was determined by filling powder (2.00 g) into a graduated measuring cylinder (10.0 mL), followed by tapping it vertically on a bench 300 times by hand.

Electrochemical characterization.—The negative electrodes were prepared by mixing active material (doped or undoped TiO₂) with a binder (polyvinylidene fluoride, PVDF, PI-KEM) and a conductive carbon (Super P, Alfa Aesar) in a ratio of 80:10:10 wt%. A 10 wt% solution of PVDF in N-methyl-2-pyrrolidone (NMP, Sigma Aldrich) was prepared using a magnetic stirrer and then mixed by hand with the conductive carbon and the active material and further NMP (ca. 2.5 mL) was added to give a viscous slurry with a solid content of ca. 20 wt%. The slurry was ball-milled at 800 rpm for 1 hour to give a consistent ink, before the ink was cast on 15 μm aluminum foil (PI-KEM). The electrode sheets were dried on a hotplate at ca. 150°C for 10 minutes until dry and then left to further dry overnight at room temperature. All electrodes were dried overnight under vacuum at 60°C before being introduced into an Ar-filled glove box for cell assembly. The active mass loadings of the negative electrodes were in the range 1.2 to 1.6 mg cm⁻². The thickness of the dried negative electrodes was in the range 35 and 45 μm.

Activated carbon positive electrodes were prepared as previously described by the authors.[35] In short, activated carbon active material (YP50F, Kuraray Chemical Co., Japan), carbon black (Super P) and PVDF (8 wt% solution in NMP) were mixed in a Buhler (Buhler Holding AG, Switzerland) high torque mixer for several hours. The ratio of active material to binder to conductive carbon was 87:8:5 wt%. The resulting ink was coated on a Megtec reel-to-reel coater in comma bar setup and passed through a three-phase oven for drying. Further drying under vacuum at 120°C for 12 hours then removed residual solvent and water. The mass loading of the positive electrodes was ca. 4.5 mg cm⁻².

The galvanostatic and potentiodynamic testing of the different TiO₂ anodes or AC cathodes in Na-ion half-cells versus metallic sodium were performed in CR2032 coin cells using a 48-channel Arbin battery tester (Model BT-2000, Caltest Instruments Ltd, Guildford, UK), at a room temperature of ca. 20°C. All testing of Na-HECs was carried out in 2-electrode Swagelok-type cells on a Gamry Interface 1000 instrument (Gamry Instruments, Pennsylvania, US). The cells were assembled in an Ar-filled glove box with O₂ and H₂O limited below 1 ppm. Whatman GF/D glass microfiber filters (Buckinghamshire, UK) were used as separator and drenched with an electrolyte (1 M NaPF₆ in 1:1 wt% ethylene carbonate/diethyl carbonate, BASF). For the half-cells, Na metal (Goodfellow Ltd) was used as counter electrode, whereas for the Na-HECs, the doped or undoped TiO₂ electrodes were used as negative electrodes, whilst the AC electrodes were used as positive electrodes. For the TiO₂ electrodes, half-cell tests were carried out in the potential window of 0.1 to 3.0 V vs. Na/Na⁺ at specific currents in the range of 0.1 to 10 A g⁻¹. The AC electrodes were tested in the potential window 2.5 to 4.0 V vs. Na/Na⁺ at specific currents in the range of 0.1 to 10 A g⁻¹. Cyclic voltammograms (CVs) for the half-cells were recorded in the potential window of 0.1 to 3.0 V vs. Na/Na⁺ for the negative electrodes and of 2.5 to 4.0 V vs. Na/Na⁺ for AC electrodes, at scan rates in the range 0.2 to 5.0 mV s⁻¹. Self-discharge testing was carried out by cycling half-cells in the potential window 0.1 to 3.0 V vs. Na/Na⁺ at a specific current of 0.5 A g⁻¹ for 9 cycles, after which the cells were left to rest under OCV conditions in their fully sodiated state for 30 h and then charge/discharge cycling was resumed. Galvanostatic Electrochemical Impedance Spectroscopy (EIS) was carried out in coin cells on a Gamry Interface 1000 instrument, in frequency range 500 kHz to 50 mHz with an AC current of 0.01 A rms.

For the Na-HECs, the CVs were performed at scan rates in the range 5 to 100 mV s^{-1} in the potential windows of 0.0 to 3.0 V, and 1.0 to 4.0 V, on two-electrode cells. Cyclic charge/discharge measurements were performed in the current density range of 0.5 to 20 mA cm^{-2}, based on the surface area of the anode (equivalent to ca. 0.1 to 4.5 A g^{-1}, based on the mass of active material in both cathode and anode). The estimated mass of active material in each electrode required for balancing of charge was determined from the results of galvanostatic half-cell measurements as described in the ESI. However, this meant that an optimized mass balance was only achieved at one specific charge/discharge rate, because the correlation between capacity and specific current differed significantly between the "battery-type" anode and double-layer capacitor cathode.[41]

Results and Discussion

Physical characterization.—After the continuous hydrothermal flow synthesis and subsequent freeze-drying of the wet solids, the nanopowders were collected with >90% yield (losses were due to unoptimized clean-up). The tap densities of the as-collected powders were 1.17, 1.32 and 1.27 g cm^{-3} for undoped TiO$_2$, Mo$_{0.1}$Ti$_{0.9}$O$_2$, and Nb$_{0.25}$Ti$_{0.75}$O$_2$, respectively. The amounts of dopants were in line with previous work for anodes in Li-ion anodes, in which they were shown to lead to improved performance.[32,35,39]

The dopant concentrations were selected because a concentration of 20 mol% of niobium precursor salt in the synthesis via CHFS was the highest dopant concentration that avoided the formation of a secondary phase (solid solubility limit in anatase). Half of that concentration (10 mol%) of molybdenum precursor salt was used to account for the fact that the difference in valence state between Ti^{4+} and Mo^{6+} was twice as high as the difference between Nb^{5+} and Ti^{4+}.

The BET specific surface areas and pore size distributions of the samples were calculated from the N$_2$ physisorption isotherms shown in Figure S2 (see ESI). The measured specific surface areas of the nanomaterials did not differ significantly between samples, and were 233.3, 238.1, and 237.2 m^2 g^{-1} for TiO$_2$, Mo$_{0.1}$Ti$_{0.9}$O$_2$ and Nb$_{0.25}$Ti$_{0.75}$O$_2$, respectively. The average pore diameter did vary more significantly, and was 11.9, 4.9, and 6.6 nm for TiO$_2$, Mo$_{0.1}$Ti$_{0.9}$O$_2$ and Nb$_{0.25}$Ti$_{0.75}$O$_2$, respectively. The pore volumes for the doped samples were also smaller compared to the pure TiO$_2$.

Structural information on the materials was gained via powder XRD and Raman spectroscopy. PXRD patterns for all as-prepared powders have been reported elsewhere,[35] and can be seen in Figure S3 (see ESI). The patterns were in good agreement with JCPDS reference card no. 071-1167 (corresponding to phase pure anatase with

Table II. Lattice parameters a and c, and the cell volume V for TiO$_2$, Mo$_{0.1}$Ti$_{0.9}$O$_2$, and Nb$_{0.25}$Ti$_{0.75}$O$_2$.

	a [/Å]	c [/Å]	V [/Å^3]
TiO$_2$	3.7809	9.5143	135.77
Mo$_{0.1}$Ti$_{0.9}$O$_2$	3.8228	9.4116	137.54
Nb$_{0.25}$Ti$_{0.75}$O$_2$	3.7983	9.4881	136.89

no impurity peaks). A small shift of peak positions to lower 2θ values was observed for the peaks at higher 2θ values, most likely caused by a small lattice expansion. The homogenous doping of anatase with Nb^{5+} or Mo^{6+} was expected to cause an expansion of the unit cell due to their higher ionic radii compared to Ti^{4+}.[42] The lattice parameters and cell volumes of the different samples were determined via refinement and indicated an expansion of the unit cell, from 135.77 Å^3 for TiO$_2$ to 137.54 and 136.89 Å^3 for Mo$_{0.1}$Ti$_{0.9}$O$_2$ and Nb$_{0.25}$Ti$_{0.75}$O$_2$, respectively (see Table II). Nb^{5+} and Mo^{6+} were expected to replace Ti^{4+} in the anatase lattice, which led to the creation of one Ti^{4+} vacancy per four Nb^{5+} or two Mo^{6+}. This has previously been reported for the doping of anatase with V^{5+} or Mo^{6+}.[43,44]

The Raman spectra of the materials are shown in Figure 1a. For undoped TiO$_2$, peaks were observed at 149 (E$_g$), 198 (E$_g$) 398 (B$_{1g}$), 516 (B$_{1g}$+A$_{1g}$), and 644 cm^{-1} (E$_g$), and were in good agreement with the expected six Raman-active modes for anatase.[45] No peaks ascribed to rutile TiO$_2$, or niobium or molybdenum oxides, were observed in any Raman spectra. Upon doping titania with either Nb^{5+} or Mo^{6+}, the main peak at 149 cm^{-1} was shifted to slightly higher wavenumbers, which could indicate a change in the O-Ti-O bending vibration, which was consistent with previously reported work on Nb-doped anatase.[46] Changes in the anatase peak positions and intensities can be related to a number of factors which could include both particle size[47] and dopants. The peak width of the E$_g$ peak at 149 cm^{-1} also increased for the doped samples, which has previously been ascribed to the formation of Nb-O-Ti and Mo-O-Ti bonds.[48] The shift to lower wave numbers and increased intensity of the E$_g$ peak at 644 cm^{-1} could be explained by the formation of Nb–O and Mo-O bonds.[48]

The valence states of the metal ions were determined by high-resolution XPS. The Ti2p level binding energies were nearly identical for all samples at ca. 459.2 and 465.0 eV for Ti 2p$_{3/2}$ and Ti 2p$_{1/2}$, respectively (see Figure 1b). These binding energies, with a spin-orbital splitting of ca. 5.8 eV, were in good agreement with the core levels of Ti^{4+}. For the doped samples, only a minimal shift to higher
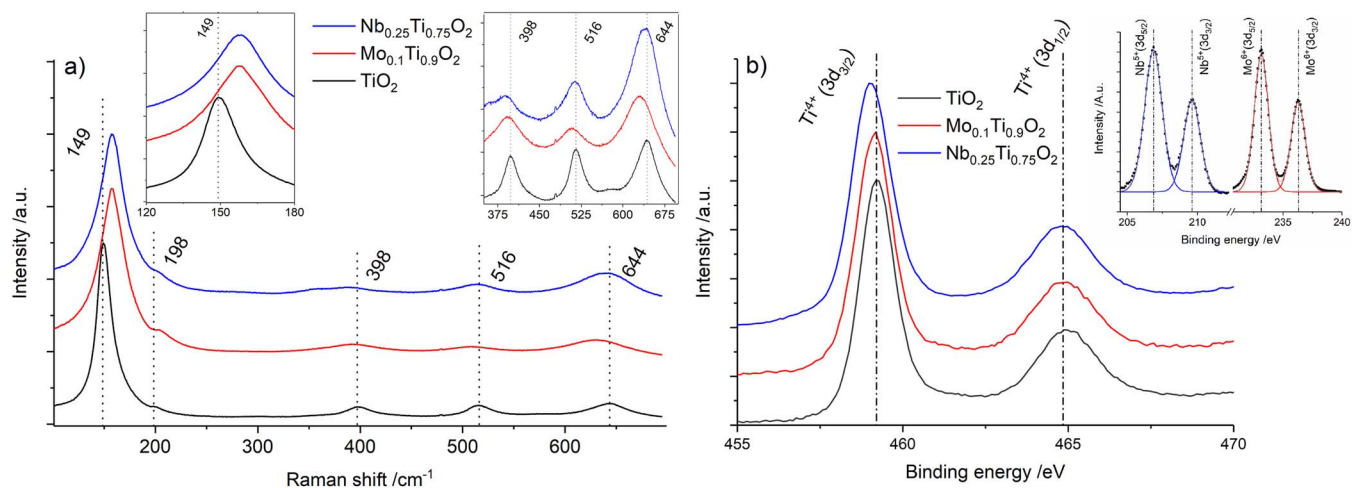

Figure 1. a) Raman spectroscopy measurements showing the significant peak shift for the doped samples with insets for the peaks at 149 and 398, 516 and 644 cm^{-1}. b) High resolution X-ray photoelectron spectroscopy (XPS) spectra for the Ti2p as well as Mo3d and Nb3d binding energy levels for the respective doped samples (inset), with data points and fitted curves.

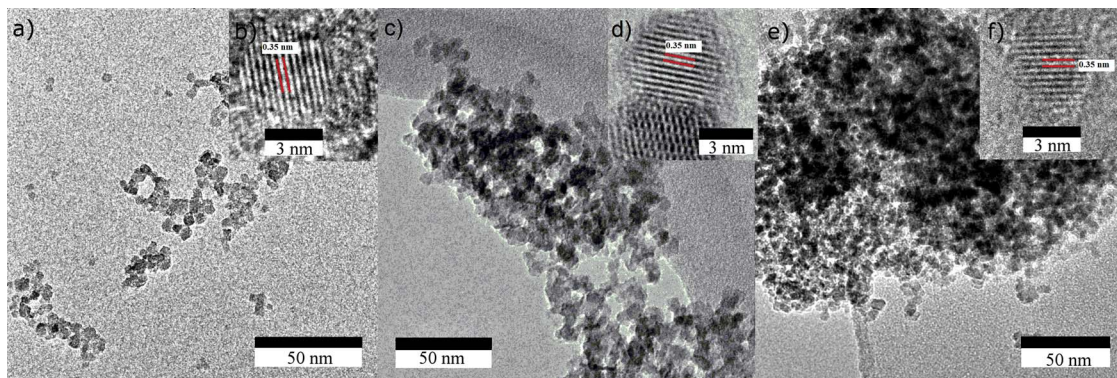**Figure 2.** Transmission electron microscopy (TEM) images showing an overview of particles of a) TiO_2, c) $Mo_{0.1}Ti_{0.9}O_2$ and e) $Nb_{0.25}Ti_{0.75}O_2$, as well as images showing lattice fringes for b) TiO_2, d) $Mo_{0.1}Ti_{0.9}O_2$ and f) $Nb_{0.25}Ti_{0.75}O_2$.

binding energy levels was observed. This, along with the unchanged symmetry of the peaks, indicated that no reduced titanium species were present after doping.[45] For the $Mo_{0.1}Ti_{0.9}O_2$ sample (see Figure 1b inset), the peaks for the dopant were located at binding energies of 236.3 and 233.2 eV for Mo $3d_{5/2}$ and Mo $3d_{3/2}$, respectively, with a spin-orbit splitting of 3.1 eV. This was in good agreement with the core levels of Mo^{6+}.[49] For the $Nb_{0.25}Ti_{0.75}O_2$ sample, high-resolution spectra showed peaks at binding energies of 207.9 and 210.7 eV for Nb $3d_{5/2}$ and Nb $3d_{3/2}$, respectively, with a spin-orbit splitting of 2.8 eV (assigned to Nb^{5+}). There were no additional peaks in the high-resolution spectra for the dopants, which indicated a single valence state for the dopant species in each case. Because of the charge imbalance implied by these chemical formulas, cationic vacancies were expected, as previously reported for anatase doped with high-valence cation dopants.[43] This was supported by the fact that the semi-quantitative analysis of XPS peak areas showed 72 and 75 at% oxygen for $Mo_{0.1}Ti_{0.9}O_2$ and $Nb_{0.25}Ti_{0.75}O_2$, respectively; more than the 67 at% expected. The atom ratios of Mo:Ti and Nb:Ti were 12:88 and 21:79, respectively.

Transmission electron microscopy revealed that particle morphology and size did not differ significantly between undoped and doped TiO_2 samples (see Figure 2). Average particle sizes were ca. 5 nm for all samples. The interlayer spacing of 0.35 nm corresponding to the (101) interplanar distances of anatase was observed for all samples (see Figures 2a, 2d, 2f). Energy-dispersive X-ray spectroscopy

found homogenously distributed dopant ions in the anatase particles and showed ca. 25 at% Nb^{5+} and 10 at% Mo^{6+} ions in the respective doped anatase samples (see Figure S4).

Electrochemical characterization of Na-ion half-cells.—The sodium-ion storage properties of the individual electrodes, including the AC positive electrodes, were separately evaluated in Na-ion half-cells (vs. Na-metal) before construction of Na-HECs. The AC positive electrodes showed the expected capacitive behavior in cyclic voltammetry at a scan rate of 0.2 mV s^{-1}, resulting in nearly rectangular voltammograms (see Figure 3a). At a moderately high specific current of 0.2 A g^{-1}, AC electrodes showed a specific capacitance of ca. 62 F g^{-1} (see Figure 3b).

Cyclic voltammograms of Na-ion half-cells at different scan rates for the various TiO_2 samples were used to examine the intercalation and pseudocapacitive charge storage behavior of the electrodes (see Figure 4). At a scan rate of 0.2 mV s^{-1}, the cathodic and anodic peaks appeared at ca. 0.5 and 1.0, 0.5 and 0.9 as well as 0.5 and 0.9 V vs. Na/Na^+, for TiO_2 (Figure 4a), $Mo_{0.1}Ti_{0.9}O_2$ (Figure 4b), and $Nb_{0.25}Ti_{0.75}O_2$ (Figure 4c), respectively (see Figure S5a). Whilst it was difficult to determine the precise position of the cathodic peak (Na$^+$ insertion) for the Nb–doped sample at higher scan rates (e.g. 5 mV s^{-1}), the position of the anodic (Na$^+$ extraction) peak shifted the most for the undoped sample (to ca. 1.75 V vs. Na/Na^+), whilst those for both the Mo-doped and Nb-doped samples also shifted to significantly
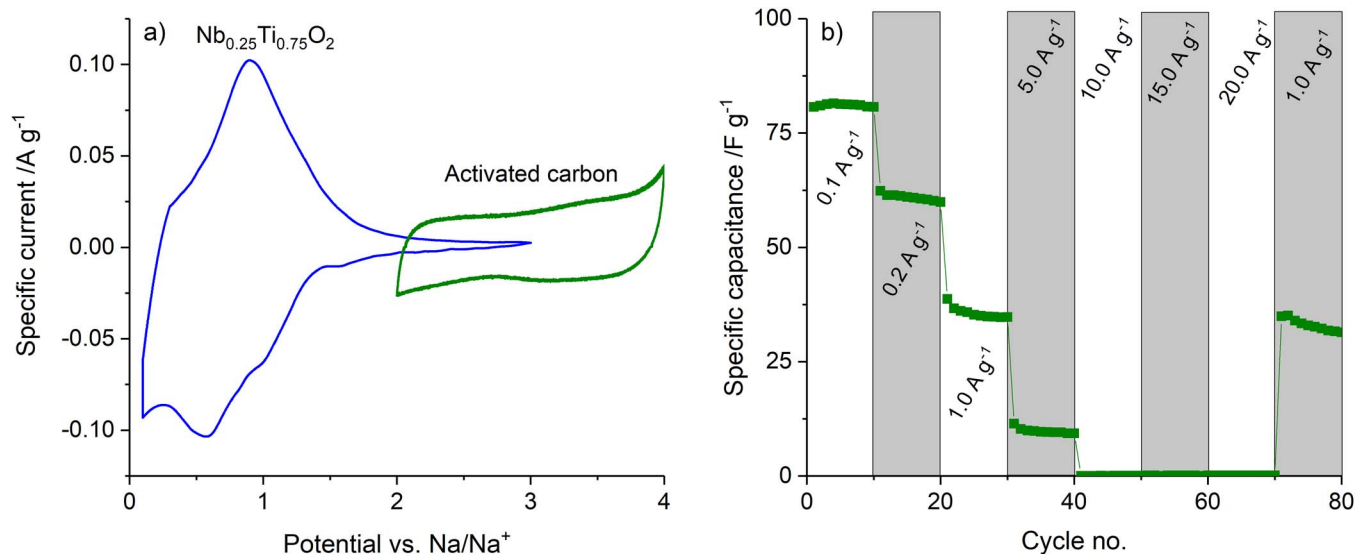

Figure 3. a) Comparison of cyclic voltammograms at a scan rate of 0.2 mV s^{-1} of a $Nb_{0.25}Ti_{0.75}O_2$ and an AC electrode in Na-ion half-cell. b) Galvanostatic charge/discharge capacitance for an AC electrode at varying applied specific currents.
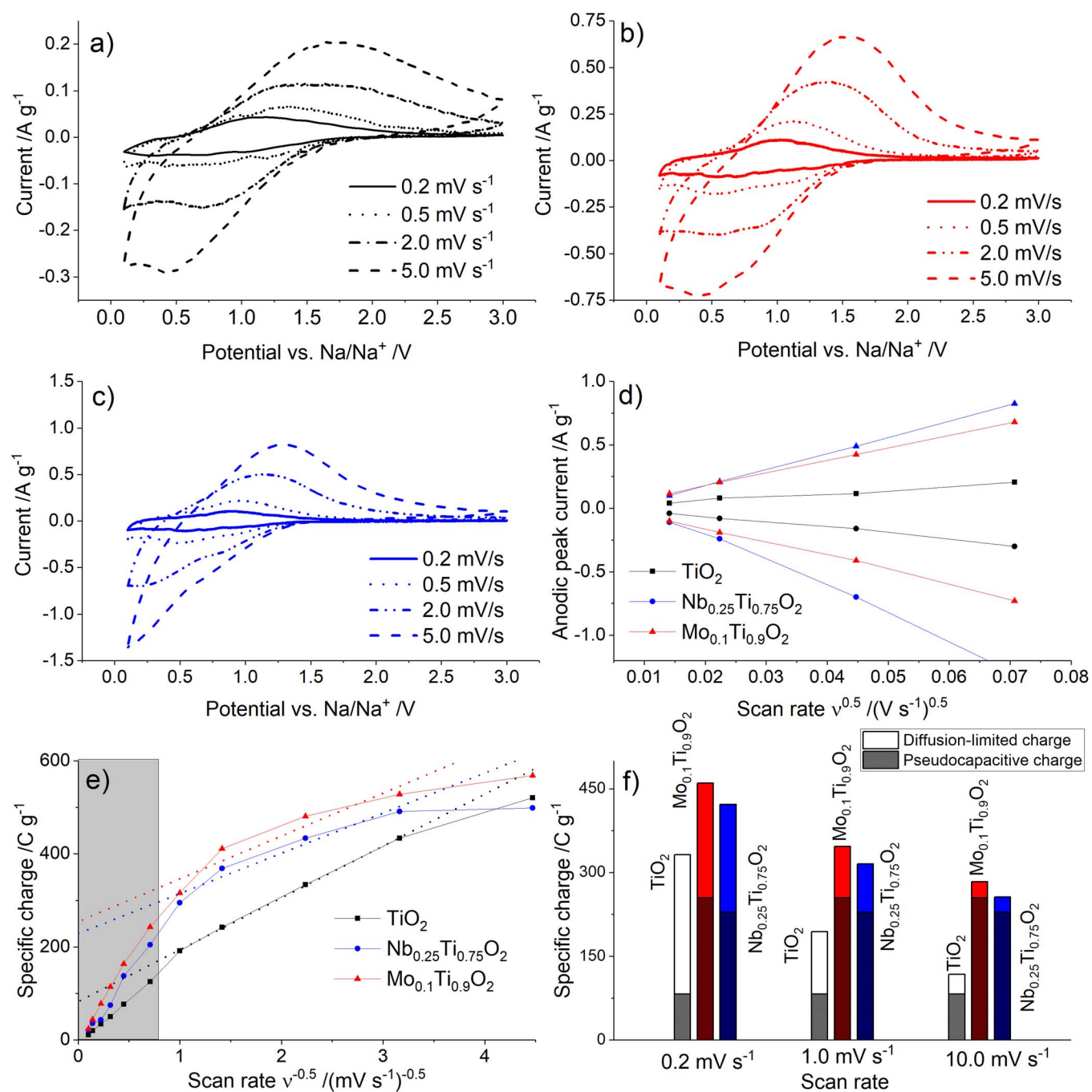
Figure 4. Cyclic voltammograms for a) TiO_2, b) $Mo_{0.1}Ti_{0.9}O_2$ and c) $Nb_{0.25}Ti_{0.75}O_2$ and d) a plot of the peak anodic and cathodic currents over the square root of the scan rate. e) Plot of specific charge versus the reciprocal of the square root of the scan rate and f) contributions from diffusion limited and pseudocapacitive charge storage to the total specific charge.

higher potentials (to ca. 1.55 and 1.25 V vs. Na/Na$^+$, respectively). This could indicate less favorable sodium-ion kinetics due to mass transport limitations in the undoped sample.[50] At the high scan rates, the peaks broadened significantly, and voltammograms became more rectangular, akin to the profile expected for materials exhibiting extrinsic pseudocapacitive charge storage properties.[27] The specific peak currents observed for the doped samples were significantly higher at faster scan rates, indicating better charge storage at higher rates (Figure 4d).

A smaller increase in peak separation for the doped samples indicated less dependence on mass transport-limited redox reactions.[14] To better understand the average overpotential at different scan rates, the

average potentials vs. Na/Na$^+$ of sodiation and desodiation were determined from capacity/voltage plots at different scan rates and plotted in Figure S5b (see supplementary information). This showed that the difference between average sodiation and desodiation potentials in a range of scan rates of 0.2 to 5.0 mV s^{-1} was consistently lower for the doped samples than for the undoped TiO_2, which was in line with the lower overpotentials determined from galvanostatic charge/discharge cycling at varying specific currents (see Figure S7).

The Randles-Sevcik method (see ESI) was used to calculate apparent Na-ion diffusion coefficients for both anodic and cathodic redox processes from anodic and cathodic peak currents, respectively, for all samples in Na-ion half-cells. The apparent specific sodium ion
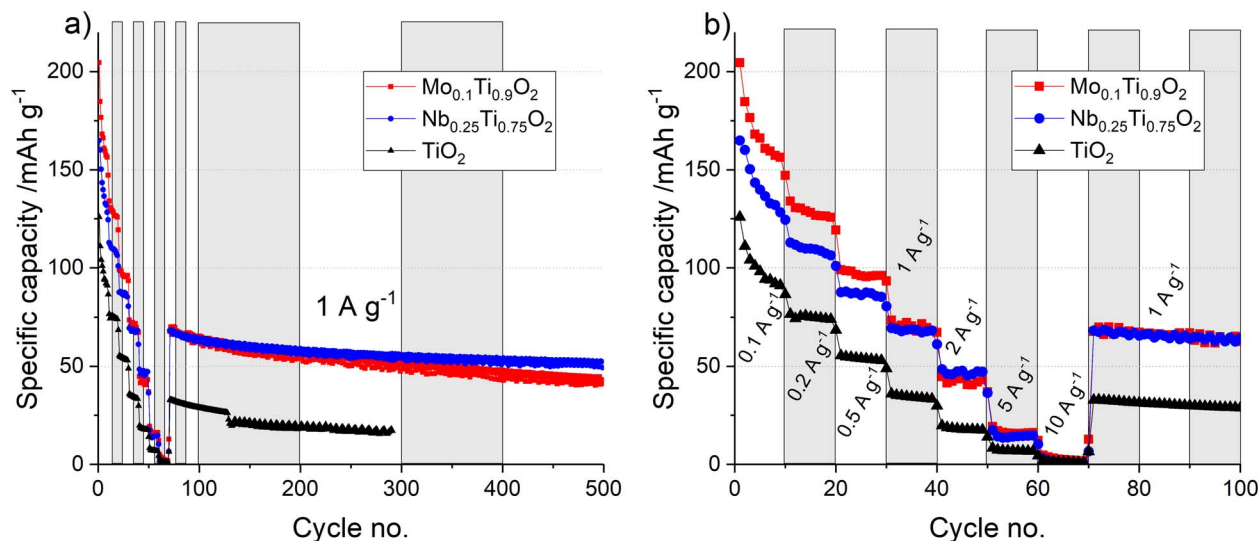
Figure 5. Charge/discharge testing at varying specific currents for a) hundreds and b) tens of cycles in Na-ion half-cells.

diffusion coefficients both for anodic and cathodic redox processes were significantly higher for $Mo_{0.1}Ti_{0.9}O_2$ (3.6 and 3.4 × 10^{-10} cm^2 s^{-1} g^{-1}, respectively) and $Nb_{0.25}Ti_{0.75}O_2$ (4.3 and 8.2 × 10^{-10} cm^2 s^{-1} g^{-1}, respectively) than for the undoped sample (3.8 and 5.6 × 10^{-11} cm^2 s^{-1} g^{-1}, respectively). Additionally, doping was expected to improve the electronic conductivity of Mo- or Nb-doped TiO_2 compared to undoped TiO_2, which has a large bandgap of 3.2 eV,[33] by introducing induced conduction band electrons, as has previously been described for Mo- and Nb-doped TiO_2.[31,32]

The proportion of pseudocapacitive and diffusion-limited charge storage contributions were separated for all samples by application of the method introduced by Trasatti (see Equation S7 in the ESI).[20,51] At a scan rate of 0.2 mV s^{-1}, this analysis yielded estimated pseudocapacitive contributions of 25, 55 and 54% to the total charge storage for TiO_2, $Mo_{0.1}Ti_{0.9}O_2$ and $Nb_{0.25}Ti_{0.75}O_2$, respectively (see Figures 4e and 4f). The pseudocapacitive charge storage contributions at 1.0 and 10.0 mV s^{-1} were 42 and 70% for TiO_2, 72 and 90% for $Mo_{0.1}Ti_{0.9}O_2$, and 73 and 89% for $Nb_{0.25}Ti_{0.75}O_2$, respectively. Because of the faster nature of pseudocapacitive charge storage compared to charge storage via diffusion-limited intercalation, these results indicated superior rate behavior for the two doped samples.[14,20] This was also in good agreement with previous findings for these nanomaterials in Li-ion half-cells.[32,35]

The specific capacities at various current rates for all samples in Na-ion half-cells were plotted in Figures 5a and 5b. At a specific current of 0.1 A g^{-1}, the initial specific capacities were ca. 125, 205 and 165 mAh g^{-1} for TiO_2, $Mo_{0.1}Ti_{0.9}O_2$ and $Nb_{0.25}Ti_{0.75}O_2$ electrodes, respectively. After 10 cycles, these had reduced to 85, 155 and 125 mAh g^{-1}, respectively. At higher specific currents of 1 A g^{-1}, the doped samples showed good rate retention with specific capacities of ca. 75 mAh g^{-1}, whereas the specific capacity of undoped TiO_2 reduced to 30 mAh g^{-1}. After cycling at higher specific currents and returning the specific current to 1 A g^{-1}, the specific capacity values returned to ca. 75 and 30 mAh g^{-1}, respectively. After >400 cycles at 1 A g^{-1}, the specific capacities had decreased to ca. 45 and 50 mAh g^{-1} for $Mo_{0.1}Ti_{0.9}O_2$ and $Nb_{0.25}Ti_{0.75}O_2$, respectively.

To investigate the improved performance of the doped TiO_2 samples compared to the undoped sample in Na-ion half-cells further, electrochemical impedance spectroscopy (EIS) was carried out at open circuit voltage (see Figure S6). The high-frequency intercept with the real impedance axis, which was a measure of the solution resistance for the cells (but especially the electrolyte and separator), was similar in all samples due to the consistent test conditions (6 to 7 Ω). The charge transfer resistances were significantly lower for the two doped samples (but especially for $Nb_{0.25}Ti_{0.75}O_2$) than

for undoped TiO_2, as previously observed for Nb-doped anatase.[16] The peak of the high-frequency semicircle, which gave an indication of electrode impedance, was at significantly lower impedances for the doped samples (at ca. 27 Ω) than for the undoped TiO_2 (at ca. 62 Ω). This was in good agreement with previous findings for Nb-doped TiO_2 in Li-ion half-cells.[32] It was also in line with trends in Na-ion diffusion coefficients between the doped and undoped samples. The diffusion coefficients in the solids was calculated using the Warburg impedance coefficients ($\sigma_{warburg}$) obtained during fitting in Equation 1:[52]

$$D = 0.5 \left(\frac{RT}{AF^2 \sigma_{warburg} C} \right)^2 \qquad [1]$$

Where D is the diffusion coefficient, R the gas constant, T the absolute temperature, A the area of the interface between electrode and electrolyte (simplified as the geometric area of the electrodes), F Faraday's constant, and C the concentration of Na-ions in the electrolyte. The diffusion coefficients were 1.05, 2.88 and 5.61 × 10^{-11} cm^2 s^{-1} for TiO_2, $Mo_{0.1}Ti_{0.9}O_2$ and $Nb_{0.25}Ti_{0.75}O_2$, respectively. These diffusion coefficients showed the same trend as those obtained from CVs but differed significantly with regards to the absolute values. Such a discrepancy has previously been observed in other studies for materials such as $Li_3V_2(PO)_4$, $Li_4Ti_5O_{12}$, and $LiVPO_4F$.[53] The discrepancy of diffusion coefficients determined via EIS and CVs was ascribed to the fact that the real geometric area of the electrode depended on the surface area of the electrode materials, and that the change in local ion concentration in the electrolyte upon cycling was ignored.[53]

The charge/discharge curves for all samples in Na-ion half-cells revealed no plateaus, at any specific current (see Figure S7a, S7b and S7c). This indicated that there was no two-phase intercalation reaction. Because of the small size of the nanoparticles, they showed a reduced (or no) miscibility gap when accommodating Na$^+$ into their structure (see Figure S7d). Similar profiles have been observed for other TiO_2 nanoparticles in the literature.[4,6,12] Also described as extrinsic pseudocapacitance, it occurred only due to electrode/material design (nanosizing), and was a result of diffusion only happening on very short distances.[25] This has previously been shown in Li-ion half cells; once a critical crystallite size was reached, a number of surface sites became available for Li$^+$ accommodation in a range of energies via fast faradaic reactions.[24,26] This has been described as the nanomaterial's surface acting as a "solid-solution host" for Li-ion storage, as the free energy of the surface changes with the concentration of Li-ions on the surface, leading to a sloped charge/discharge profile.[27] This critical crystallite size for solid-solution host behavior has been

demonstrated, amongst others, for $LiCoO_2$,[54] and TiO_2.[55] Due to the comparable behavior of the samples in this study, their surface can therefore be interpreted as "solid-solution surface hosts" for Na-ions. This behavior can only be achieved in nanoparticles because of the high available surface area.

The charge/discharge profiles revealed superior charge storage properties for the doped samples compared to the undoped TiO_2 electrodes. This combined with the lower peak separation for the doped samples found in the cyclic voltammograms showed the beneficial effect of doping anatase on Na-ion storage behavior. This was supported by the average potential difference between sodiation and desodiation in half-cells, which increased from ca. 0.5 V for $Mo_{0.1}Ti_{0.9}O_2$ and $Nb_{0.25}Ti_{0.75}O_2$ at 0.1 A g^{-1}, to 1.7 V at 5.0 A g^{-1}. The potential difference was higher at all specific currents for undoped TiO_2 (0.6 and 1.9 V at 0.1 and 5.0 A g^{-1}, respectively).

Potential step chronoamperometry of the Na-ion half-cells revealed similar profiles for all samples, with currents during sodiation significantly higher for a potential step from 0.8 to 0.1 V vs. Na/Na$^+$ than at higher potentials, and currents significantly higher for a potential step from 0.8 to 1.5 V vs. Na/Na$^+$ for the desodiation than at lower potentials (see Figure S8a, S8b, S8c, and S8d), which was in line with the observations on average sodiation and desodiation potentials.

A self-discharge test for the Na-ion half-cells was carried out with a self-discharge step (monitoring of OCV) of 30 h. Self-discharge over this time was calculated to be 20% of discharge capacity for $Mo_{0.1}Ti_{0.9}O_2$ and 22% for both TiO_2 and $Nb_{0.25}Ti_{0.75}O_2$. This was a less pronounced fall in capacity than has previously been observed for carbon anodes in Na-ion half-cells.[56] The fall in Coulombic efficiencies due to self-discharge showed similar values for all samples. However, there was no appreciable irreversible self-discharge for any sample, both discharge capacities and Coulombic efficiencies regained previous values on the next discharge (see Figure S9a). There was little noticeable difference in the discharge curves for the samples between the 9th (last cycle before self-discharge step) and the 11th cycle (first cycle after self-discharge step) for all samples (see Figure S9b).

Electrochemical characterization of Na-ion hybrid electrochemical capacitors.—Because of their promising charge storage behavior in Na-ion half-cells, especially at high current rates, the $Mo_{0.1}Ti_{0.9}O_2$ and the $Nb_{0.25}Ti_{0.75}O_2$ electrodes were used in Na-HECs with activated carbon (AC) cathodes. The non-optimized mass ratio of active material in the negative and positive electrodes was ca. 1:4, determined from the charge stored by both individual electrodes (see Supplementary Information and Figure S10). This was in line with previous work on Li-HECs,[35] and was supported by charge/discharge measurements for both AC and doped TiO_2 samples in their active potential range (see Figure S11).

The electrochemical performance of the Na-HECs was studied using galvanostatic charge/discharge measurements. The cell specific capacitance was calculated using Equations 2 and 3:

$$C_{cell} = (I\,t)\,/\Delta V\,m \qquad [2]$$

$$\Delta V = E_{max} - E_{min} \qquad [3]$$

Where I was the charge current (A), t was the discharge time (s), ΔV was the potential window (V), and m was the mass of active material in both the anode and cathode (g). E_{max} and E_{min} were the potentials at the beginning and at the end of the discharge cycle.

The Na-HECs were cycled in the ranges 0.0 to 3.0 V and 1.0 to 4.0 V in the current density range 0.5 to 20 mA cm^{-2}, which was equivalent to specific currents in the range of ca. 0.1 to 4.5 A g^{-1}, based on the mass of active material in both anode and cathode. Because of the lower sodiation and desodiation potential vs. Na/Na$^+$ compared to lithiation and delithiation potentials vs. Li/Li$^+$ for TiO_2, cycling a Na-HEC up to as high as 4.0 V was possible (see Figure S11).[57] This compares favorably to the upper potential for Li-HECs, which are typically only cycled to 3.0 V because of the higher electrochemical potential of TiO_2 vs. Li/Li$^+$. Because sodiation activity of

TiO_2 began at ca. 1.5 V vs. Na/Na$^+$, whereas AC can be active as positive electrode >2.5 V vs. Na/Na$^+$, there is very limited charge storage to be expected in the potential window of 0 to 1 V. This might explain limited performance for some capacitors previously reported.[28] For reference only, the cycling data for Na-HECs cycled in the range 0.0 to 3.0 V can be found in the ESI (see Figure S12).

The charge/discharge profiles of the Na-HECs at current densities of 0.5, 1, 5, 10 and 20 mA cm^{-2} are shown in Figures 6a and 6b. The curves at all current densities deviated slightly from the expected triangular shape for purely electric double-layer capacitors as has previously been observed for Na-HECs,[28] and been attributed to fast faradaic reaction in the anode.[29,30] This was as expected, because a combination of faradaic and non-faradaic charge storage mechanisms were active for such a redox-pseudocapacitor type anode and EDLC-type cathode.[58] During charging, faradaic reactions of sodium cations with TiO_2 and hexafluorophosphate anion adsorption onto the active carbon in the positive electrode were expected, whereas discharge was expected to result in PF$_6{}^-$ desorption and Na$^+$ extraction from TiO_2.[20,21]

The specific discharge capacitances for Na-HECs containing $Nb_{0.25}Ti_{0.75}O_2$/AC were 24, 20, 16, 13 and 11 F g^{-1} (ca. 20, 17, 11, 9 and 6 mAh g^{-1}, respectively) at current densities of 0.5, 1, 5, 10 and 20 mA cm^{-2}, respectively (see Figure S13c). The specific capacitances for the $Mo_{0.1}Ti_{0.9}O_2$/AC Na-HECs were slightly higher than those for the Nb-doped sample, with specific capacitances of 26, 21, 16, 15 and 13 F g^{-1} (22, 17, 11, 9 and 6 mAh g^{-1}) at current densities of 0.5, 1, 5, 10 and 20 mA cm^{-2}, respectively (see Figure 6c). The Coulombic efficiency in the 10 initial cycles at 0.5 mA cm^{-2} was between 80 and 90%, probably due to the formation of SEI, but rose quickly to 99% at 5 mA cm^{-2}. In good agreement with the results from measurements in Na-ion half cells, the Na-HECs using undoped TiO_2 active material performed significantly worse than those using the doped samples, with specific capacitances of 14, 8 and 3 F g^{-1} (12, 7 and 2 mAh g^{-1}) at current densities of 0.5, 1, and 5 mA cm^{-2}, respectively (see Figure S13a and S13b).

The cyclic voltammograms of the Na-HECs showed profiles that resembled the optimal (rectangular) form for a capacitor, but also a mixture of the separate electrode profiles (see Figure S14b, S14c, and S14d). At high scan rates, there were more distinctive peaks, as previously observed for similar devices.[59,60] This indicated imperfect anode/cathode active mass balancing for higher scan rates. The cyclic voltammograms for Na-HECs were also used to calculate the specific capacitances of the devices (C_{cell}) at different scan rates using Equation 4:

$$C_{cell} = q/\,(\Delta V\,m) \qquad [4]$$

Where q was the charge (C), ΔV was the potential window (V) and m was the mass of active material in both the anode and cathode (g).

These results were in good agreement with the capacitances calculated from galvanostatic charge/discharge measurements above. Mo-doped TiO_2 Na-HECs showed the highest capacitance of 30 F g^{-1} at 5 mV s^{-1} (see Figure S14a, equivalent to 25 mAh g^{-1}), whilst the capacitance of the capacitor using Nb-doped TiO_2 as anode material was 27 F g^{-1} (equivalent to 22 mAh g^{-1}). The $Mo_{0.1}Ti_{0.9}O_2$/AC Na-HECs also retained capacitance well, showing a capacitance of ca. 13 F g^{-1} (10 mAh g^{-1}) compared to ca. 14 F g^{-1} (11 mAh g^{-1}) at a scan rate of 100 mV s^{-1} for the $Nb_{0.25}Ti_{0.75}O_2$/AC Na-HEC, and just 23 and 6 F g^{-1} for TiO_2/AC Na-HECs at 5 and 100 mV s^{-1}, respectively. However, the $Mo_{0.1}Ti_{0.9}O_2$/AC Na-HEC also showed a rapid decline in capacitance with increasing scan rate, similar to the TiO_2/AC Na-HEC. This could have been a result of less perfect active mass balancing due to the difference in charge-dependence between anode and cathode. More significant SEI formation could also have played a role.

When Na-HECs were cycled at 10 mA cm^{-2}, the specific capacity was most stable for $Mo_{0.1}Ti_{0.9}O_2$/AC Na-HEC after 3000 cycles with high Coulombic efficiencies (>99% initially, falling to >98.5%, which was higher than at lower current densities reported above, due to limited SEI formation) as shown in Figure S13d. The
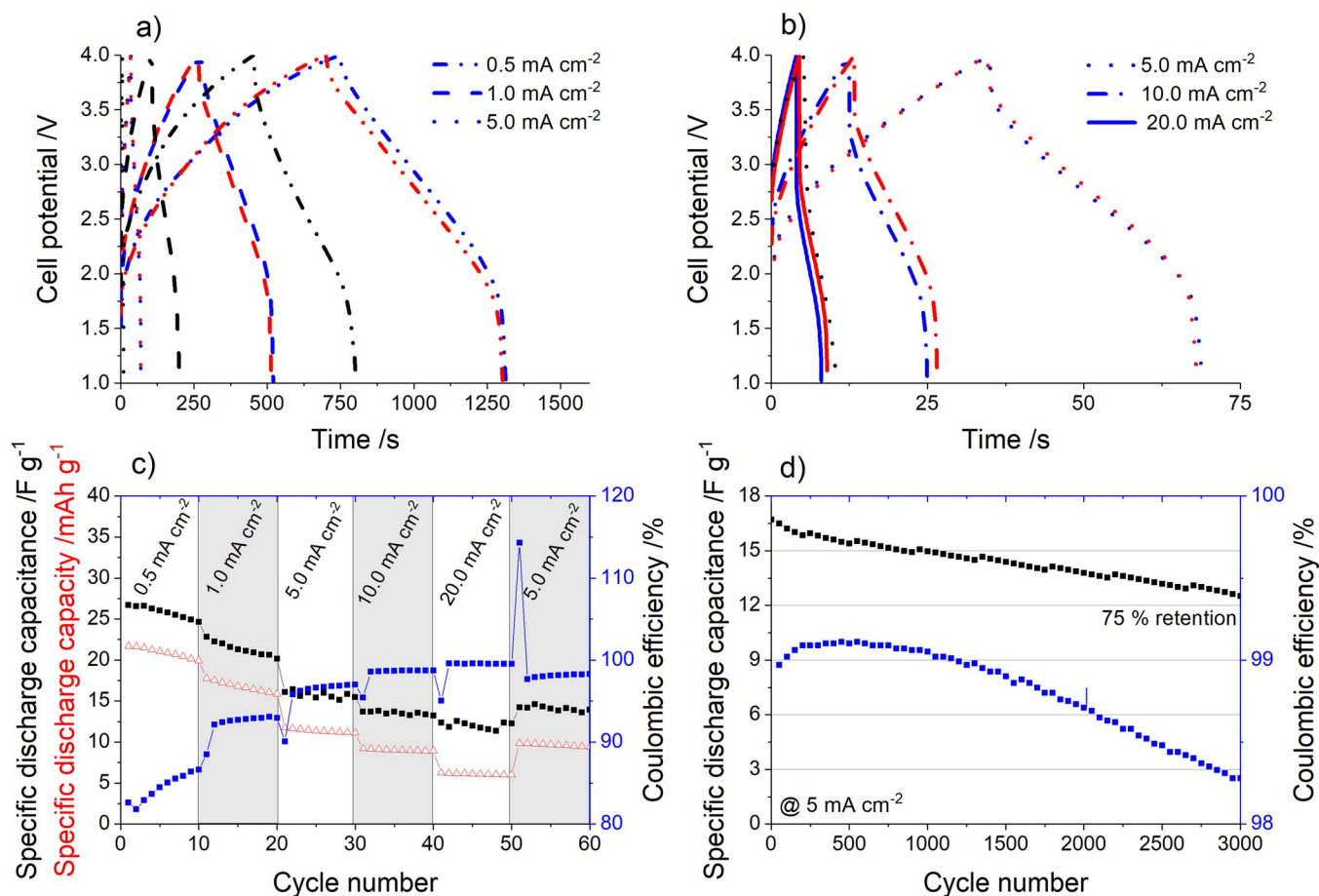
Figure 6. a) and b) Cyclic charge/discharge profiles for TiO_2/AC, $Mo_{0.1}Ti_{0.9}O_2/AC$ and $Nb_{0.25}Ti_{0.75}O_2/AC$ Na-HECs in black, red and blue, respectively, at various current densities. c) Specific capacitance and specific capacity of $Mo_{0.1}Ti_{0.9}O_2/AC$ hybrid Na-ion capacitors. d) Long term cycling data for $Nb_{0.25}Ti_{0.75}O_2/AC$ hybrid Na-ion capacitors.

$Nb_{0.25}Ti_{0.75}O_2/AC$ Na-HEC showed a specific capacitance retention of ca. 75% (see Figure 6d). This was similarly stable as some previously reported Na-HECs such as $NiCo_2O_4/AC$,[28] Na-titanate/AC,[29] or N-doped TiO_2/AC.[57]

Energy density (*E*) and power density (*P*) were calculated using Equations 5 and 6:

$$P = \Delta V \ (I/m) \qquad [5]$$

$$E = P \ (t/3600) \qquad [6]$$

ΔV was the average potential during discharge calculated from the discharge curves, *I* was the current (A), *m* was the mass of the active materials in both anode and cathode (kg) and *t* was the discharge time (s).

$Mo_{0.1}Ti_{0.9}O_2/AC$ Na-HECs delivered the highest observed energy density of 60 Wh kg^{-1} at a power density of 350 W kg^{-1} (see Figure 7). They also retained energy density best at higher power densities and showed energy densities of 31 and 13 Wh kg^{-1} at power densities of 3360 and 10650 W kg^{-1}, respectively. The $Nb_{0.25}Ti_{0.75}O_2/AC$ Na-HECs performed well, especially at intermediate power densities, showing energy densities of 21 Wh kg^{-1} at a power density of 6000 W kg^{-1}. The TiO_2/AC Na-HEC, on the other hand, showed significantly lower energy densities of 31 and 3 Wh kg^{-1} at moderate power densities of 322 and 2350 W kg^{-1}, respectively.

To compare the performance of the Na-HECs herein with other reports of similar systems from the literature, the energy and power densities for devices such as $NiCoO_2/AC$,[28] AC/Na-titanate,[29] AC/AC,[29] $Na_4Mn_9O_{18}/AC$,[30] $V_2O_5/CNT-AC$,[20] $Nb_2O_5@C/AC$,[61] Na-

TNT/graphite,[62] Na-TNT/AC,[62] and $Na_2Ti_2O_4(OH)_2$/Porous carbon[63] Na-ion (hybrid) capacitors were added to the Ragone plot in Figure 7. This demonstrated the excellent performance of the Na-HECs presented herein compared to similar devices.

Conclusions

Titania nanoparticles doped with either niobium or molybdenum were synthesized via continuous hydrothermal flow synthesis and studied as active materials for anodes in Na-ion batteries and Na-ion hybrid capacitors. The high surface area of the nanomaterials allowed near-surface pseudocapacitive charge storage, and higher sodium-ion diffusion coefficients in the doped samples led to notably higher specific capacities at high specific currents compared to undoped TiO_2.

$Mo_{0.1}Ti_{0.9}O_2$ electrodes in Na-ion half-cells showed specific capacities of >150 mAh g^{-1} after 10 cycles at 0.1 A g^{-1}, whereas at 1 A g^{-1}, the specific discharge capacities were still high at ca. 75 mAh g^{-1} for both doped samples, which was more than double that of undoped titania electrodes under the same conditions.

Because of the excellent charge storage properties at high applied currents, Na-ion hybrid electrochemical capacitors using doped titania negative electrodes and activated carbon positive electrodes were produced. The $Mo_{0.1}Ti_{0.9}O_2/AC$ Na-HECs showed the highest observed energy densities of 60 Wh kg^{-1} at a power density of 350 W kg^{-1} and performed the best at the highest power density of 10650 W kg^{-1}, at which it still showed an energy density of 13 Wh kg^{-1}.

The work herein has clearly shown the promising properties of nanomaterials synthesized via CHFS and their adaptability from Li-ion battery applications to other energy storage applications such as
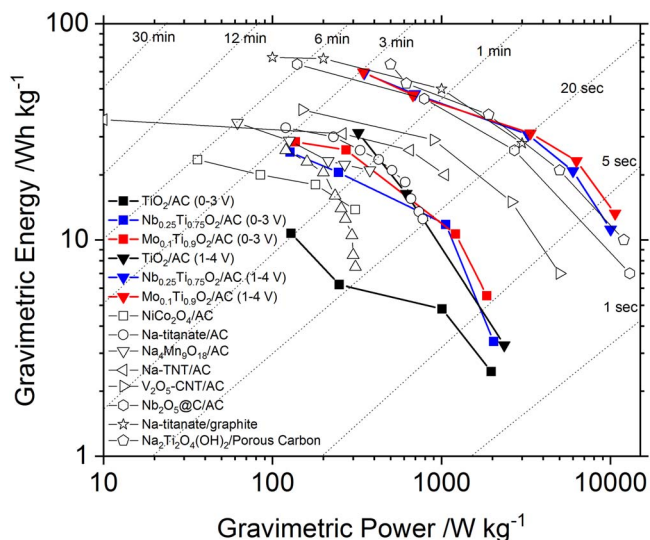
Figure 7. Ragone plot comparing the performance of the Na-HECs with similar devices from the literature such as NiCoO$_2$/AC,[28] AC/Na-titanate,[29] AC/AC,[29] Na$_4$Mn$_9$O$_{18}$/AC,[30] V$_2$O$_5$/CNT-AC,[20] Nb$_2$O$_5$@C/AC,[61] Na-TNT/graphite,[62] Na-TNT/AC,[62] and Na$_2$Ti$_2$O$_4$(OH)$_2$/Porous carbon[63] Na-ion (hybrid) capacitors.

Na-ion batteries and Na-HECs. The high surface area of these materials and consistent doping at high concentrations played an important role due to the importance of surface-near charge storage in both Li-ion and Na-ion applications. As the CHFS method is highly scalable, it should be possible to manufacture larger devices; the results of these efforts will be reported in due course.

ORCID

Dan J. L. Brett https://orcid.org/0000-0002-8545-3126
Paul R. Shearing https://orcid.org/0000-0002-1387-9531
Emma Kendrick https://orcid.org/0000-0002-4219-964X
Noriyoshi Matsumi https://orcid.org/0000-0003-3621-5313
Jawwad A. Darr https://orcid.org/0000-0002-1076-3162

References

1. M. Armand and J.-M. Tarascon, *Nature*, **451**, 652 (2008).
2. J. M. Tarascon and M. Armand, *Nature*, **414**, 359 (2001).
3. M. R. Palacín, *Chem. Soc. Rev.*, **38**, 2565 (2009).
4. Y. Xu, E. M. Lotfabad, H. Wang, B. Farbod, Z. Xu, A. Kohandehghan, and D. Mitlin, *Chem. Commun.*, **49**, 8973 (2013).
5. H. Usui, S. Yoshioka, K. Wasada, M. Shimizu, and H. Sakaguchi, *ACS Appl. Mater. Interfaces*, **7**, 6567 (2015).
6. L. Wu, D. Buchholz, D. Bresser, L. Gomes Chagas, and S. Passerini, *J. Power Sources*, **251**, 379 (2014).
7. D. A. Stevens and J. R. Dahn, *J. Electrochem. Soc.*, **147**, 1271 (2000).
8. L. Xiao, Y. Cao, W. A. Henderson, M. L. Sushko, Y. Shao, J. Xiao, W. Wang, M. H. Engelhard, Z. Nie, and J. Liu, *Nano Energy*, **19**, 279 (2016).
9. D. Bresser, F. Mueller, D. Buchholz, E. Paillard, and S. Passerini, *Electrochim. Acta*, **128**, 163 (2013).
10. Y. Xu, Y. Zhu, Y. Liu, and C. Wang, *Adv. Energy Mater.*, **3**, 128 (2013).
11. R. Alcantara, M. Jaraba, P. Lavela, and J. L. Tirado, *Chem. Mater.*, **14**, 2847 (2002).
12. H. Xiong, M. D. Slater, M. Balasubramanian, C. S. Johnson, and T. Rajh, *J. Phys. Chem. Lett.*, **2**, 2560 (2011).
13. Z. Bi, M. P. Paranthaman, P. A. Menchhofer, R. R. Dehoff, C. A. Bridges, M. Chi, B. Guo, X. G. Sun, and S. Dai, *J. Power Sources*, **222**, 461 (2013).
14. C. Chen, Y. Wen, X. Hu, X. Ji, M. Yan, L. Mai, P. Hu, B. Shan, and Y. Huang, *Nat. Commun.*, **6**, 6929 (2015).
15. L. Wu, D. Bresser, D. Buchholz, and S. Passerini, *J. Electrochem. Soc.*, **162**, A3052 (2014).
16. F. Zhao, B. Wang, Y. Tang, H. Huang, H. Ge, and H. Liu, *J. Mater. Chem. A*, **3**, 22969 (2015).
17. W. Song, H. Zhao, L. Wang, S. Liu, and Z. Li, *ChemElectroChem*, **5**, 316 (2018).
18. H. Ibrahim, A. Ilinca, and J. Perron, *Renew. Sustain. Energy Rev.*, **12**, 1221 (2008).
19. A. Lewandowski, P. Jakobczyk, M. Galinski, and M. Biegun, *Phys. Chem. Chem. Phys.*, **15**, 8692 (2013).
20. Z. Chen, V. Augustyn, X. Jia, Q. Xiao, B. Dunn, and Y. Lu, *ACS Nano*, **6**, 4319 (2012).
21. R. Zuo, R. Li, C. Zhou, Y. Li, J. Xia, and J. Liu, *Adv. Sci.*, **4**, 1600539 (2017).
22. V. Aravindan, J. Gnanaraj, Y.-S. Lee, and S. Madhavi, *Chem. Rev.*, **114**, 11619 (2014).
23. Z. Hong, K. Zhou, Z. Huang, and M. Wei, *Sci. Rep.*, **5**, 11960 (2015).
24. V. Augustyn, P. Simon, and B. Dunn, *Energy Environ. Sci.*, **7**, 1597 (2014).
25. T. Brousse, D. Belanger, and J. W. Long, *J. Electrochem. Soc.*, **162**, A5185 (2015).
26. J. Come, V. Augustyn, J. W. Kim, P. Rozier, P.-L. Taberna, P. Gogotsi, J. W. Long, B. Dunn, and P. Simon, *J. Electrochem. Soc.*, **161**, A718 (2014).
27. A. G. Dylla, G. Henkelman, and K. J. Stevenson, *Acc. Chem. Res.*, **46**, 1104 (2013).
28. R. Ding, L. Qi, and H. Wang, *Electrochim. Acta*, **114**, 726 (2013).
29. J. Yin, L. Qi, and H. Wang, *ACS Appl. Mater. Interfaces*, **4**, 2762 (2012).
30. X. Liu, N. Zhang, J. Ni, and L. Gao, *J. Solid State Electrochem.*, **17**, 1939 (2013).
31. H. Liao, L. Xie, Y. Zhang, X. Qiu, S. Li, Z. Huang, H. Hou, and X. Ji, *Electrochim. Acta*, **219**, 227 (2016).
32. M. Lübke, J. Shin, P. Marchand, D. Brett, P. Shearing, Z. Liu, and J. A. Darr, *J. Mater. Chem. A*, **3**, 22908 (2015).
33. Y.-C. Nah, I. Paramasivam, and P. Schmuki, *ChemPhysChem*, **11**, 2698 (2010).
34. A. Byeon, M. Boota, M. Beidaghi, K. V. Aken, J. W. Lee, and Y. Gogotsi, *Electrochem. commun.*, **60**, 199 (2015).
35. D. Bauer, A. J. Roberts, N. Matsumi, and J. A. Darr, *Nanotechnology*, **28**, 195403 (2017).
36. Y. Furubayashi, T. Hitosugi, Y. Yamamoto, K. Inaba, G. Kinoda, Y. Hirose, T. Shimada, and T. Hasegawa, *Appl. Phys. Lett.*, **86**, 1 (2005).
37. R. I. Gruar, C. J. Tighe, and J. A. Darr, *Ind. Eng. Chem. Res.*, **52**, 5270 (2013).
38. J. A. Darr, J. Zhang, N. M. Makwana, and X. Weng, *Chem. Rev.*, **117**, 11125 (2017).
39. D. Bauer, A. J. Roberts, C. L. Starkey, R. Vedarajan, D. J. L. Brett, P. R. Shearing, N. Matsumi, and J. A. Darr, *Int. J. Electrochem. Sci.*, **13**, 5120 (2018).
40. D. P. Howard, P. Marchand, I. D. Johnson, C. J. Carmalt, I. P. Parkin, and J. A. Darr, *J. Mater. Chem. A*, **4**, 12774 (2016).
41. C. T. Hsu, C. C. Hu, T. H. Wu, J. C. Chen, and M. Rajkumar, *Electrochim. Acta*, **146**, 759 (2014).
42. J. Zhang, T. Huang, L. Zhang, and A. Yu, *J. Phys. Chem. C*, **118**, 25300 (2014).
43. L. T. Anh, A. K. Rai, T. V. Thi, J. Gim, S. Kim, E. C. Shin, J. S. Lee, and J. Kim, *J. Power Sources*, **243**, 891 (2013).
44. T. V. Thi, A. K. Rai, J. Gim, S. Kim, and J. Kim, *J. Alloys Compd.*, **598**, 16 (2014).
45. S. Sharma, S. Chaudhary, S. C. Kashyap, and S. K. Sharma, *J. Appl. Phys.*, **109** (2011).
46. A. J. Gardecka, G. K. L. Goh, G. Sankar, and I. P. Parkin, *J. Mater. Chem. A*, **3**, 17755 (2015).
47. Z. Zhang, S. Brown, J. B. M. Goodall, X. Weng, K. Thompson, K. Gong, S. Kellici, R. J. H. Clark, J. R. G. Evans, and J. A. Darr, *J. Alloys Compd.*, **476**, 451 (2009).
48. H. Su, Y. T. Huang, Y. H. Chang, P. Zhai, N. Y. Hau, P. C. H. Cheung, W. T. Yeh, T. C. Wei, and S. P. Feng, *Electrochim. Acta*, **182**, 230 (2015).
49. W. Ji, R. Shen, R. Yang, G. Yu, X. Guo, L. Peng, and W. Ding, *J. Mater. Chem. A*, **2**, 699 (2014).
50. C.-Y. Lee and A. M. Bond, *Langmuir*, **26**, 16155 (2010).
51. S. Ardizzone, G. Fregonara, and S. Trasatti, *Electrochim. Acta*, **35**, 263 (1990).
52. B. Tian, H. Xiang, L. Zhang, Z. Li, and H. Wang, *Electrochim. Acta*, **55**, 5453 (2010).
53. J. Wang, X. Li, Z. Wang, H. Guo, B. Huang, Z. Wang, and G. Yan, *J. Solid State Electrochem.*, **19**, 153 (2015).
54. M. Okubo, E. Hosono, J. Kim, M. Enomoto, N. Kojima, T. Kudo, H. Zhou, and I. Honma, *J. Am. Chem. Soc.*, **129**, 7444 (2007).
55. J. Wang, J. Polleux, J. Lim, and B. Dunn, *J. Phys. Chem. C*, **111**, 14925 (2007).
56. R. Mogensen, D. Brandell, and R. Younesi, *ACS Energy Lett.*, **1**, 1173 (2016).
57. S. Liu, Z. Cai, J. Zhou, A. Pan, and S. Liang, *J. Mater. Chem. A*, **4**, 18278 (2016).
58. V. Aravindan, W. Chuiling, and S. Madhavi, *J. Mater. Chem.*, **22**, 16026 (2012).
59. H. Kim, M.-Y. Cho, M.-H. Kim, K.-Y. Park, H. Gwon, Y. Lee, K. C. Roh, and K. Kang, *Adv. Energy Mater.*, **3**, 1500 (2013).
60. N. Nitta, F. Wu, J. T. Lee, and G. Yushin, *Mater. Today*, **18**, 252 (2014).
61. E. Lim, J. Changshin, M. S. Kim, M. H. Kim, J. Chun, H. Kim, J. Park, K. C. Roh, K. Kang, S. Yoon, and J. Lee, *Adv. Funct. Mater.*, **26**, 3711 (2016).
62. L. Zhao, L. Qi, and H. Wang, *J. Power Sources*, **242**, 597 (2013).
63. B. Babu and M. M. Shaijumon, *J. Power Sources*, **353**, 85 (2017).